Physics of the Earth and Planetary Interiors 235 (2014) 33–48

Contents lists available at ScienceDirect

Physics of the Earth and Planetary Interiors

journal homepage: www.elsevier.com/locate/pepi

Radially anisotropic 3-D shear wave structure of the Australian lithosphere and asthenosphere from multi-mode surface waves

K. Yoshizawa

Earth and Planetary Dynamics, Department of Natural History Sciences, Faculty of Science, Hokkaido University, Sapporo 060-0810, Japan

ARTICLE INFO

Article history:
Received 29 October 2013
Received in revised form 18 July 2014
Accepted 22 July 2014
Available online 1 August 2014

Keywords:
Surface waves
Tomography
Anisotropy
Australia
Lithosphere
Asthenosphere

ABSTRACT

A new radially anisotropic shear wave speed model for the Australasian region is constructed from multi-mode phase dispersion of Love and Rayleigh waves. An automated waveform fitting technique based on a global optimization with the Neighbourhood Algorithm allows the exploitation of large numbers of three-component broad-band seismograms to extract path-specific dispersion curves covering the entire continent. A 3-D shear wave model is constructed including radial anisotropy from a set of multi-mode phase speed maps for both Love and Rayleigh waves. These maps are derived from an iterative inversion scheme incorporating the effects of ray-path bending due to lateral heterogeneity, as well as the finite frequency of the surface waves for each mode. The new S wave speed model exhibits major tectonic features of this region that are in good agreement with earlier shear wave models derived primarily from Rayleigh waves. The lateral variations of depth and thickness of the lithosphere–asthenosphere transition (LAT) are estimated from the isotropic (Voigt average) S wave speed model and its vertical gradient, which reveals correlations between the lateral variations of the LAT and radial anisotropy. The thickness of the LAT is very large beneath the Archean cratons in western Australia, whereas that in south Australia is thinner. The radial anisotropy model shows faster SH wave speed than SV beneath eastern Australia and the Coral Sea at the lithospheric depth. The faster SH anomaly in the lithosphere is also seen in the suture zone between the three cratonic blocks of Australia. One of the most conspicuous features of fast SH anisotropy is found in the asthenosphere beneath the central Australia, suggesting anisotropy induced by shear flow in the asthenosphere beneath the fast drifting Australian continent.

1. Introduction

The 3-D shear wave structure of the Australian upper mantle has been investigated by a number of researchers in the last two decades, building on a series of seismic experiments undertaken throughout Australia since the pioneering transportable seismic array project SKIPPY (van der Hilst et al., 1994). A number of Australian upper mantle models have been proposed using a variety of methods, with different styles of approximations (e.g., Debayle and Kennett, 2000a,b; Simons et al., 2002; Yoshizawa and Kennett, 2004; Fishwick et al., 2005, 2008; Fichtner et al., 2010; Fishwick and Rawlinson, 2012). These models have revealed the robust large-scale features of the continental lithosphere of Australia; i.e., faster wave speeds in the Archean and Proterozoic cratons in the West, North and South Australia (Fig. 1) and slower wave speeds in the eastern Phanerozoic margin. Most of these works have, however, been based primarily on the observations of Rayleigh waves on the vertical component of motion, and hence the shear wave models are primarily based on SV wave information.

There are only a few exceptions that constructed radially anisotropic models of Australia, incorporating Love waves (e.g., Debayle and Kennett, 2000a, 2010). Debayle and Kennett (2000a) proposed the first three-dimensional radial anisotropy model of the Australasian upper mantle from the simultaneous inversion of Love and Rayleigh waves. This early model identified the large-scale features of both isotropic S wave speed as well as radial anisotropy, although the horizontal resolution is limited since only small numbers of paths (about 800 for both Love and Rayleigh waves) were available in their mapping. More recently, Fichtner et al. (2010) obtained a 3-D radial anisotropy model working with full waveform tomography using three component seismograms. Their method is highly sophisticated in that complex wave propagation phenomena in 3-D structure can be taken into account in their modeling, though the method is computationally demanding and requires high quality three-component seismic waveform data, which tend to limit the numbers of paths (about 3000) that can be used in their tomographic mapping.

The anisotropic heterogeneity in the Australian region has also been investigated through global-scale studies (e.g., Gung et al., 2003; Debayle et al., 2005). Gung et al. (2003) revealed the

E-mail address: kazu.yoshizawa@mail.sci.hokudai.ac.jp

http://dx.doi.org/10.1016/j.pepi.2014.07.008
0031-9201/

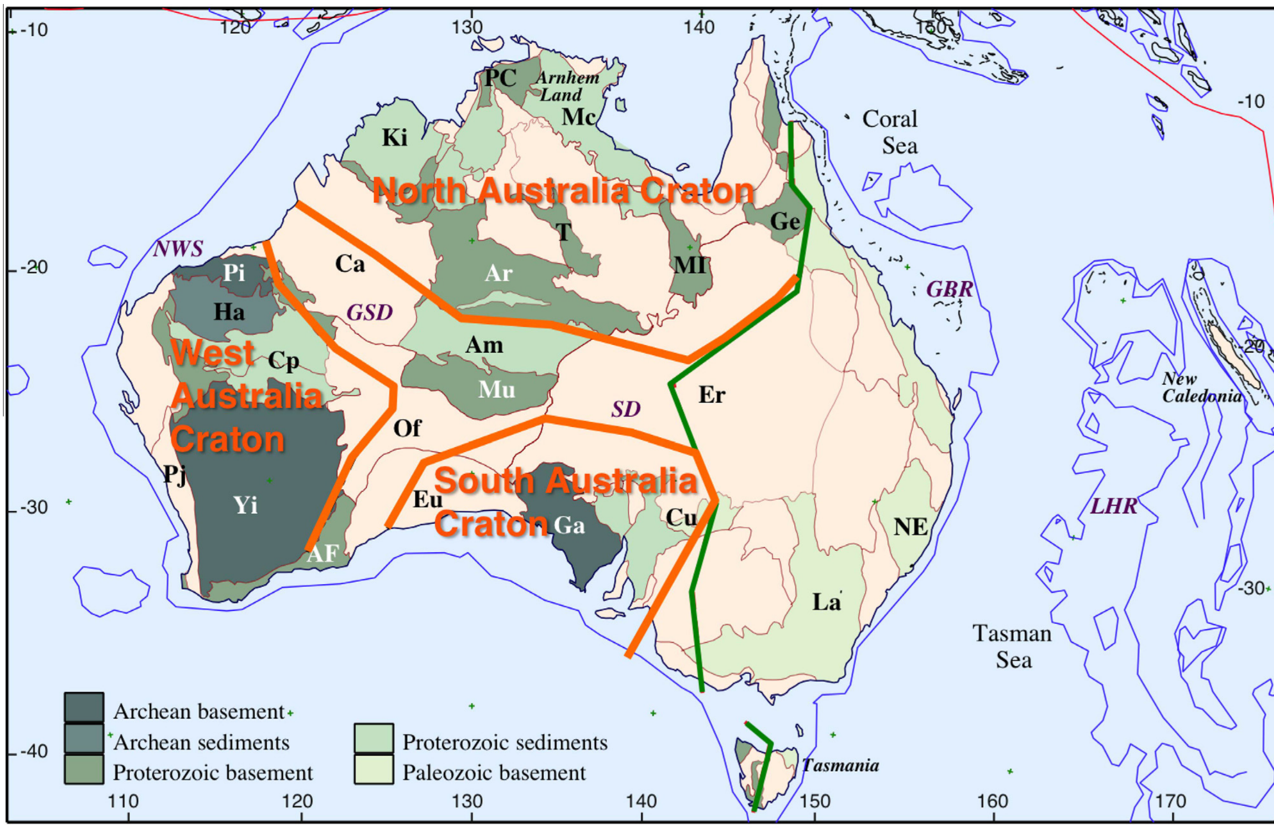

Fig. 1. A tectonic map of Australia and surrounding region. Orange solid lines represent boundaries of major cratonic blocks (North, South and West Australia Cratons) and green solid line Tasman Line. AF – Albany-Fraser belt, Ar – Arunta Block, Am – Amadeus Basin, Ca – Canning Basin, Cp – Capricorn Orogen, Cu – Curnamona Craton, Er – Eromanga Basin, Eu – Eucla Basin, Ga – Gawler Craton, Ge – Georgetown inlier, Ha – Hamersley Basin, Ki – Kimberley Block, La – Lachlan Orogen, Mc – MacArthur Basin, MI – Mt Isa Block, Mu – Musgrave Block, NE – New England Orogen, Of – Officer Basin, PC – Pine Creek Inlier, Pi – Pilbara Craton, Pj – Pinjarra Orogen, T – Tennant Creek Block, Yi – Yilgarn Craton, NWS – Northwest Shelf, GBR – Great Barrier Reef, LHR – Lord Howe Rise, SD – Simpson Desert, GSD – Great Sandy Desert. (For interpretation of the references to colour in this figure legend, the reader is referred to the web version of this article.)

existence of faster SH wave speed anomalies than SV waves beneath the continental areas. These faster anomalies of the horizontally polarized shear wave compared with the vertically polarized one were argued to represent the effects of strong shear beneath the continental lithosphere. Debayle et al. (2005) reported anomalously strong azimuthal anisotropy beneath Australian lithosphere in comparison with other continental regions, by employing a global surface wave tomography incorporating azimuthal anisotropy. Such observations are likely to reflect the lattice preferred orientation caused by the strong shear beneath the fast moving Australian continent, migrating northward with a speed of about 7 cm per year. The seismological evidence of anomalous anisotropy beneath Australia can be a key to unveiling the effects of basal drag beneath the thick continental lithosphere and tectonic history of the long-lived Archean/Proterozoic cratons that comprise the major portions of the present-day continental plate of Australia, though the global-scale models provide us with only a large-scale view of the continental upper mantle. There is, therefore, still plenty of room for the construction of a new high-resolution regional-scale 3-D model of the Australian upper mantle including radial anisotropy, encompassing the entire continent with enhanced ray coverage.

In this study, we use a large data set covering the whole Australian continent to obtain a high resolution regional 3-D radial anisotropy model of the Australasian region. We employ a three-stage inversion scheme of surface wave tomography (Kennett and Yoshizawa, 2002; Yoshizawa and Kennett, 2004) to retrieve a new three-dimensional shear wave model from multi-mode phase speeds of both Love and Rayleigh waves incorporating the effects of finite frequency and off-great-circle propagation. An earlier version of this model presented in this paper has been used as one of three models employed in the construction of the latest reference upper mantle model of Australia (AuSREM – Mantle Component) by Kennett et al. (2013).

The main objective of this paper is to retrieve the three-dimensional distribution of radially anisotropic shear wave speeds beneath the Australasian region with improved path coverage for both Love and Rayleigh waves, and to estimate the plausible depth range of the lithosphere–asthenosphere transition beneath the continent, which will be a key to the better understanding of plate tectonics and mantle dynamics underneath the long-lived and fast moving continent of Australia.

2. Data and method for multi-mode phase speed measurements

Dispersion curves of multi-mode surface waves are extracted from a fully nonlinear waveform fitting scheme (Yoshizawa and Kennett, 2002b; Yoshizawa and Ekström, 2010), based on the exploration of model parameter space using the Neighbourhood Algorithm (Sambridge, 1999). The original method developed by Yoshizawa and Kennett (2002b) has recently been improved by employing several empirical criteria to implement automatic data selection and outlier detection as described by Yoshizawa and Ekström (2010). In this section, we briefly explain the process of nonlinear waveform fitting for estimating multi-mode dispersion curves along a specific path, as well as the data set of observed phase speeds used in this study.

2.1. Method of multi-mode phase speed measurements

The first step of our three-stage surface wave tomography (Yoshizawa and Kennett, 2004) is to collect a large number of path-specific phase dispersion curves through waveform fitting by matching synthetic and observed seismograms. At this stage, we employ a path-specific 1-D shear wave speed model as a representation of the multi-mode phase dispersion. Multiple time windows for both fundamental and higher modes are used to better fit the observed and synthetic seismograms exploiting multiple band-pass filters. The filter spreads cover the total frequency range from 5 to 50 mHz for the stations affiliated to FDSN (The International Federation of Digital Seismograph Networks), and from 10 to 50 mHz for temporary regional seismic networks deployed throughout Australia by the seismology group of Australian National University.

The synthetic waveforms are calculated based on the WKBJ theory for surface waves (e.g., Dahlen and Tromp, 1998). The dispersion curves generally are robust and stable, as compared to the rather non-unique path-specific 1-D models, and are only weakly affected by the choice of the reference 1-D models or their parameterization (Yoshizawa and Kennett, 2002b).

The waveform fitting process is fully automated and the quality of the collected phase dispersion curves is evaluated quantitatively by using several empirical criteria: (1) The reliability parameter as a function of frequency that represents the degree of waveform fit and relative power of each mode in a chosen time window based on a spectrogram in time–frequency domain; (2) Outlier detection and removal through a statistical analysis based on Grubbs' test for a group of similar paths in which both the events and stations are located within a certain circular range with the radius R; in this study, we employed a radius defined by $R = L \sin\Delta$, where L is 2.5° and Δ is the epicentral distance. Details of the data selection criteria are fully described by Yoshizawa and Ekström (2010).

2.2. Data set

We used three-component broad-band seismograms of the FDSN stations from 1990 to 2007 provided by IRIS Data Management Center, as well as those of the portable seismic stations in Australia in the period from 1993 to 2004. Seismic events with moment magnitude between 5.0 and 7.5 are used in the waveform analysis. Each of the original seismograms is first deconvolved with the corresponding instrument responses, and is analyzed with the nonlinear waveform fitting scheme described in the previous section.

The events and stations used in this study, as well as the attained ray path coverage for the fundamental mode Rayleigh waves and the second higher mode Love waves are displayed in Fig. 2. The numbers of phase speed data for each mode of both Love and Rayleigh waves are plotted in Fig. 3 as a function of frequency. We have gathered more than 8000 paths for the fundamental mode Rayleigh waves for the majority of our target frequency range (less than 30 mHz), while the number of paths for higher modes are limited to about 2000 to 3000 for Rayleigh waves. The number of Love wave measurements are about two thirds of those for Rayleigh waves. We have constructed phase speed maps for all the modes and frequencies for which more than 480 paths are available. These phase speed models are then used to constrain the final 3-D shear wave model as explained in the following section.

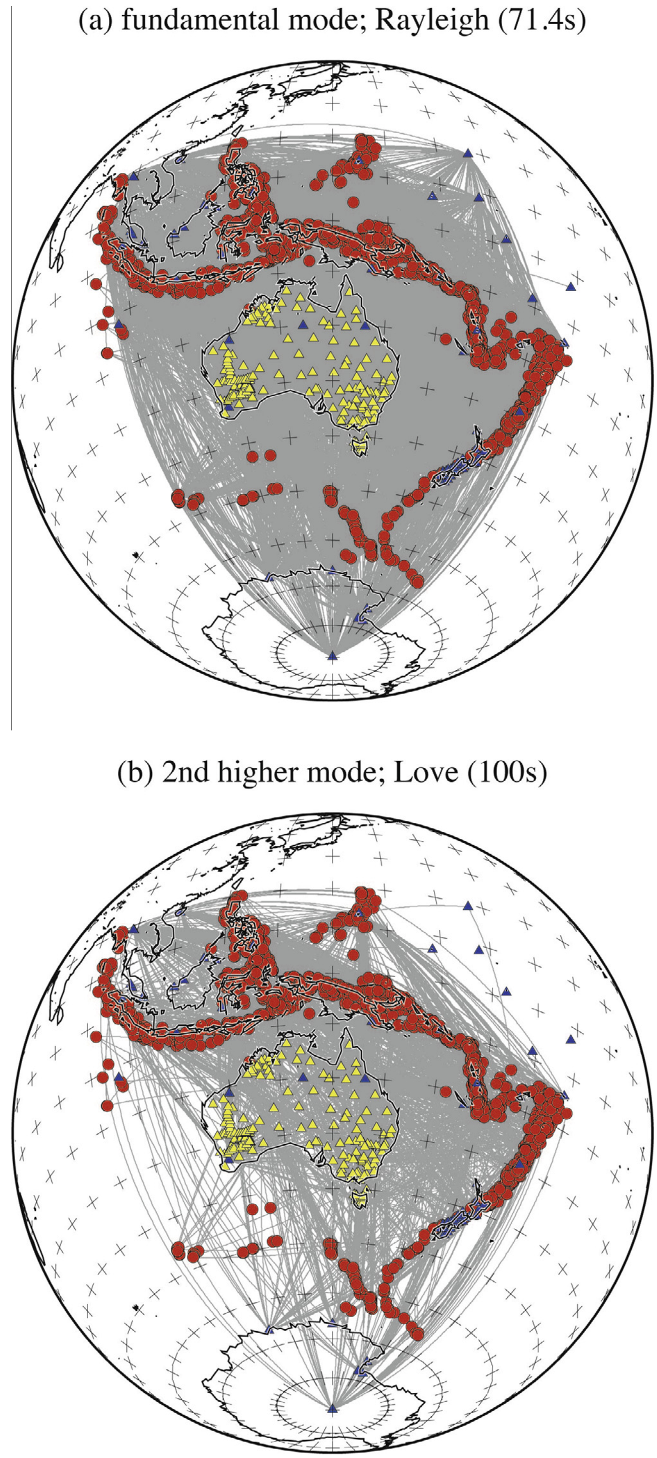

Fig. 2. The distribution of seismic events, stations and paths used in this study for (a) fundamental mode Rayleigh wave at 71.4 s period and (b) 2nd higher-mode Love wave at 100 s period. Yellow triangles indicate the transportable broad-band stations deployed by ANU, blue triangles the stations affiliated to FDSN, and red circles the employed seismic events. (For interpretation of the references to colour in this figure legend, the reader is referred to the web version of this article.)

3. Multimode phase speed maps

Path-specific phase speeds described in the previous section are used as secondary data to invert for the multi-mode phase speed models. At this second step of the three-stage surface wave tomography, we first assume finite-width rays along the great circle paths by taking account of the effects of finite-frequency around the great circle. These initial phase speed maps are then updated by incorporating the effects of off-great-circle propagation as well as the finite-frequency effects around the propagation paths based on the *influence zone* defined by Yoshizawa and Kennett (2002a).

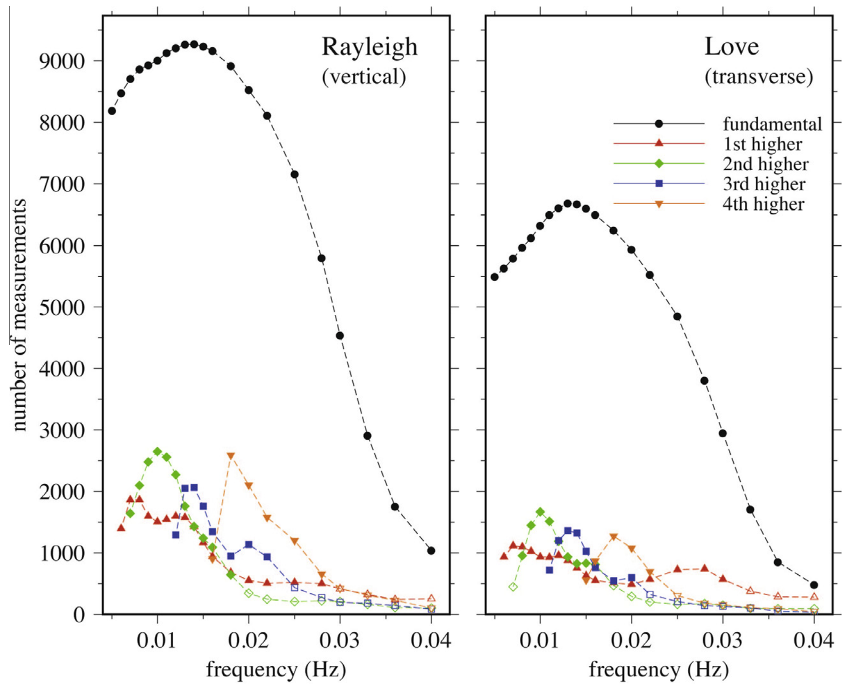

Fig. 3. Number of measurements for Rayleigh and Love waves up to the 4th higher mode as a function of frequency, after the quality control of the automated phase speed measurements. Blank symbols indicate unused data in the subsequent phase speed mapping.

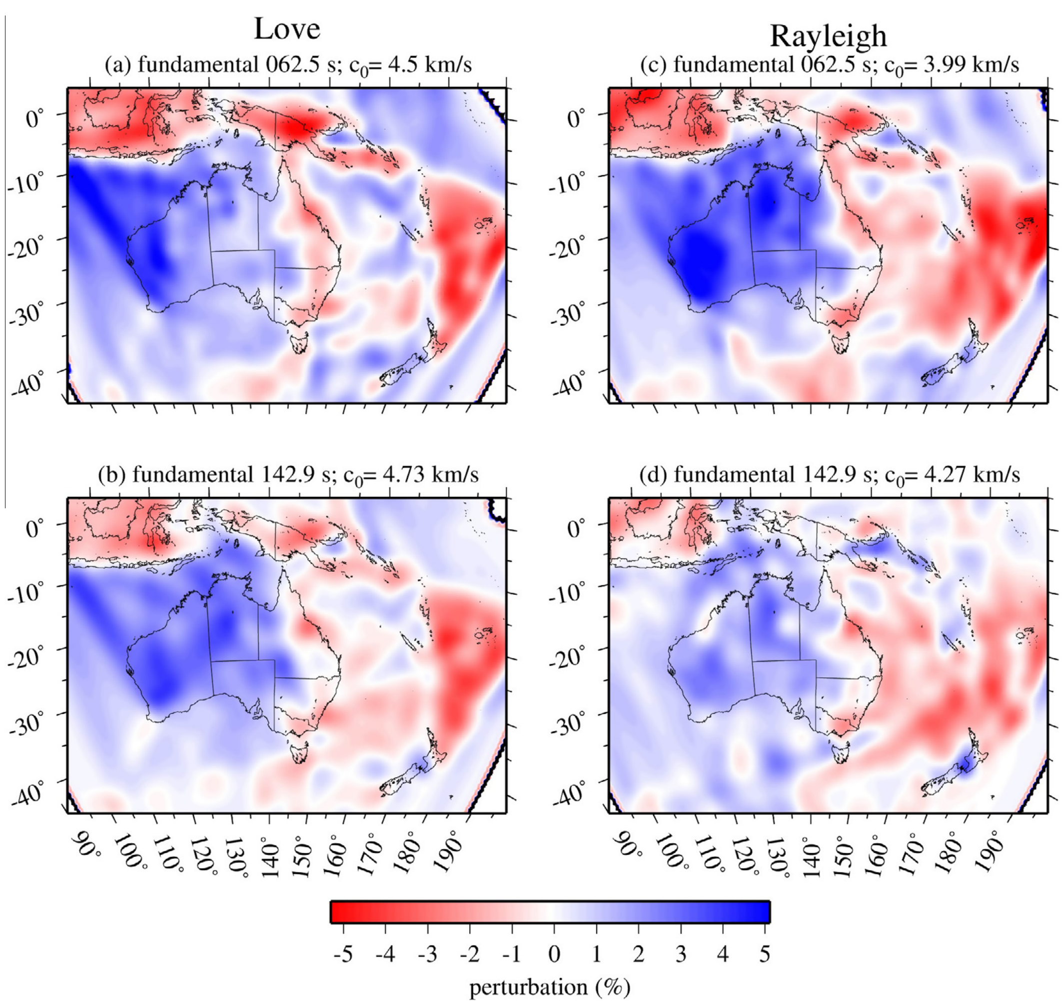

Fig. 4. Examples of phase speed maps for fundamental-mode Love and Rayleigh waves at 62.5 s and 142.9 s period.

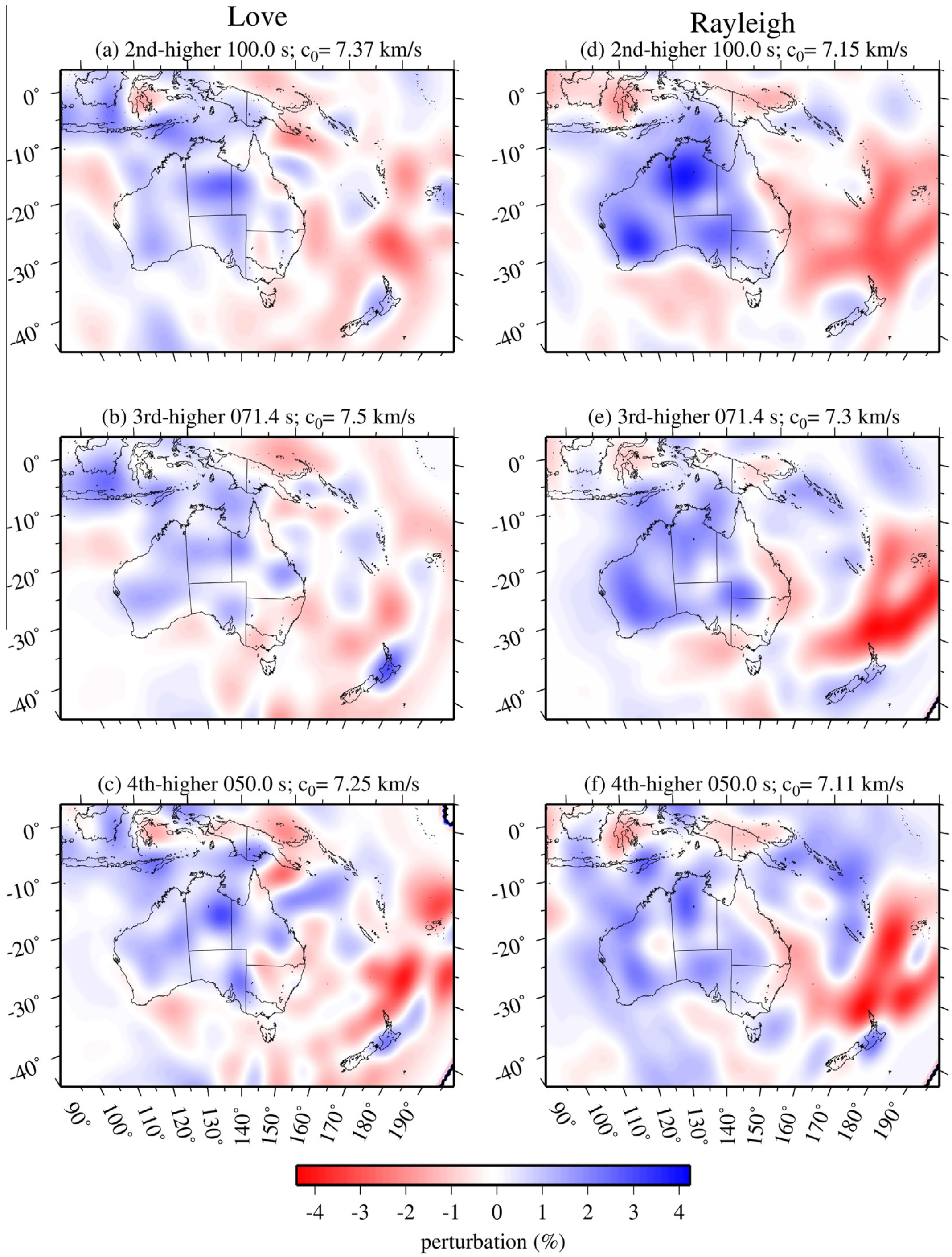

Fig. 5. Examples of phase speed maps of Love and Rayleigh waves for 2nd, 3rd and 4th higher modes.

These updated phase speed maps for each mode and frequency are used to constrain the final 3-D shear wave model.

The detailed procedure of our mapping technique is fully described by Yoshizawa and Kennett (2004). The approach has been applied to a variety of regional-scale tomographic mapping both in continental regions (e.g., Yoshizawa and Kennett, 2004; Yoshizawa and Ekström, 2010) and in oceanic regions (e.g., Isse et al., 2006b; Bourova et al., 2010). Phase speed models are expanded in a set of B-spline functions with a rectangular grid. The grid (or knot) interval used in this study varies depending on the number of paths for each mode and frequency; we used 2.0° for models with more than 5000 paths, 3.0° for over 3000 paths and 4.0° for over 480 paths.

Examples of the updated phase speed maps for the fundamental mode and the second higher mode are displayed in Figs. 4 and 5, respectively. The large scale features of fast anomalies in the cratonic blocks as well as slow wave speeds in the Tasman sea are clearly mapped in these models.

Some examples of checkerboard resolution tests are shown in Fig. 6 for the fundamental mode Rayleigh waves at 71.4 s, and in Fig. 7 for the second higher mode Rayleigh and Love waves at 100 s. The retrieved checkerboard patterns in Fig. 6 represent the achievable resolution of our phase speed models with a large number of paths for the fundamental mode, whereas those in Fig. 7 gives us an insight into the typical resolution of higher mode models with limited path coverage and with longer wavelength.

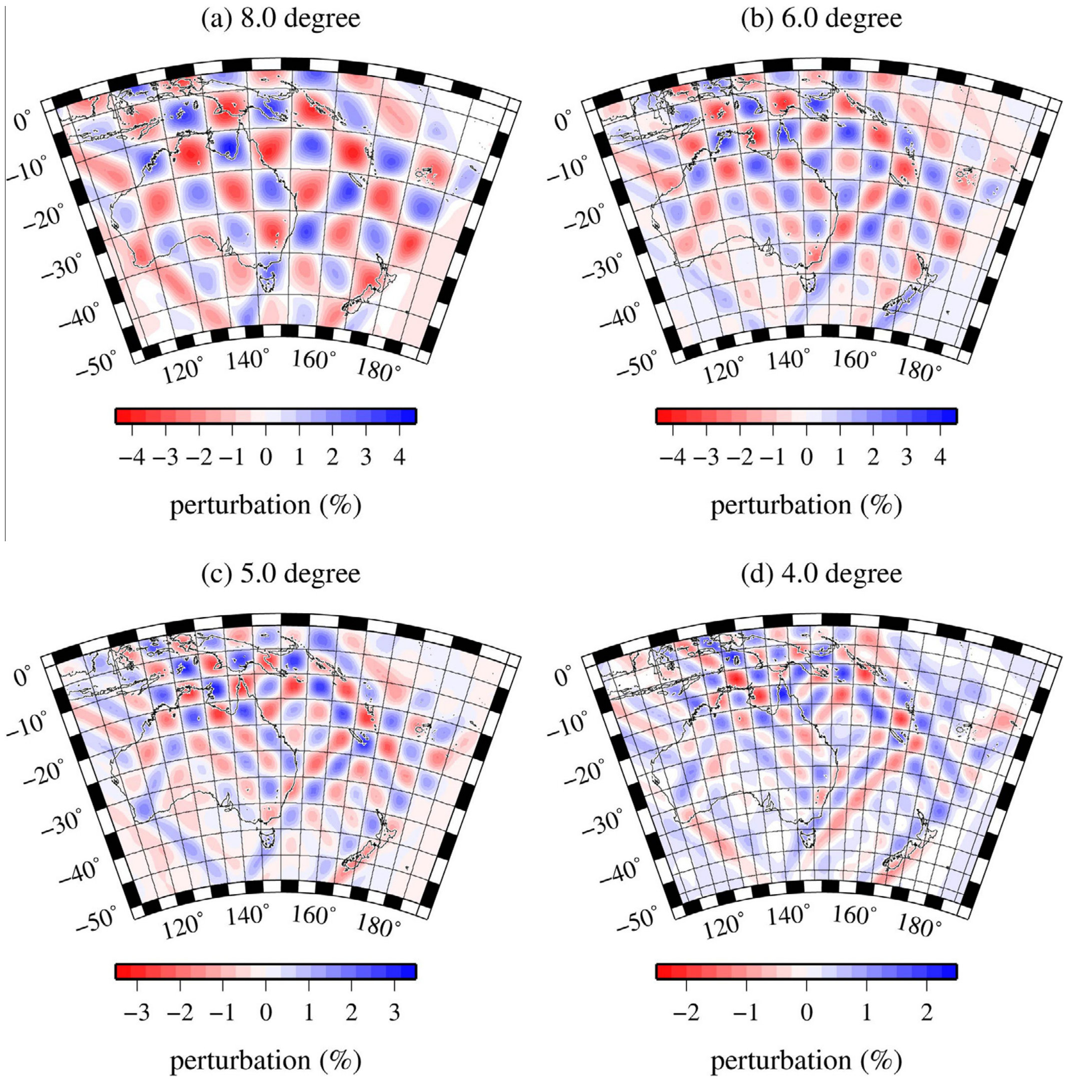

Fig. 6. Results of checkerboard tests for the fundamental-mode Rayleigh wave at 71.4 s period with (a) 8.0° cells, (b) 6.0° cells, (c) 5.0° cells and (d) 4.0° cells.

Since the Rayleigh waves on the vertical component provide us with larger numbers of better waveform fits, resulting in a large phase speed data set with better spatial coverage, the Rayleigh wave models normally achieve a better recovery of the original checkerboard patterns. Still, the Love wave models also indicate satisfactory recovery of the major portion of the heterogeneous pattern, allowing us to construct the radially anisotropic heterogeneous model of this region with the optimum horizontal resolution of about 300 km locally.

4. Radially anisotropic shear wave speed model of Australia

The multi-mode phase speed maps obtained in the previous sections are used to construct the final 3-D model incorporating radial anisotropy. In this final step, we have employed an iterative nonlinear least-squares inversion scheme by Tarantola and Valette (1982). The SV and SH wave speeds at each location are obtained by the inversion of local multi-mode phase speed data extracted from the phase speed maps, with a correction for the local crustal structure using the 3SMAC model (Nataf and Ricard, 1996). The details of the method have been described in Yoshizawa et al. (2010), but, in this study, we have employed a different parameterization for radial anisotropy as described in detail below.

4.1. Model parameterization

For the reconstruction of velocity profiles with radial anisotropy (or transverse isotropy), we may use either set of 6 independent model parameters (e.g., Takeuchi and Saito, 1972), (A) $[\rho, \alpha_H, \phi, \beta_V, \xi, \eta]$ or (B) $[\rho, \alpha_H, \alpha_V, \beta_V, \beta_H, \eta]$, where α_H and α_V represent PH (horizontally polarized P) and PV (vertically polarized P) wave speeds, β_V and β_H represent SV (vertically polarized S) and SH (horizontally polarized S) wave speeds. η is a dimensionless anisotropic parameter, $\phi = (\alpha_V/\alpha_H)^2$ and $\xi = (\beta_H/\beta_V)^2$. Either approach for model parameterization can be theoretically valid, though their resolving power for the anisotropic properties of shear wave speeds are not identical. In this study, we have used the second sets of parameterization (B) with SV and SH wave speeds, β_V and β_H, which are used as independent parameters for inversion, since the Love wave sensitivity kernels in this case exhibit better sensitivities to SH wave speeds with less effects from SV wave speeds (see the first section of electronic supplement). Also, this set of parameters provide us with smaller misfit with our dispersion data. The remaining four parameters are also taken into account through a conventional scaling relationship to shear wave parameters (e.g., Gung et al., 2003,Panning and Romanowicz, 2006) based on the work by Montagner and Anderson (1989), although the

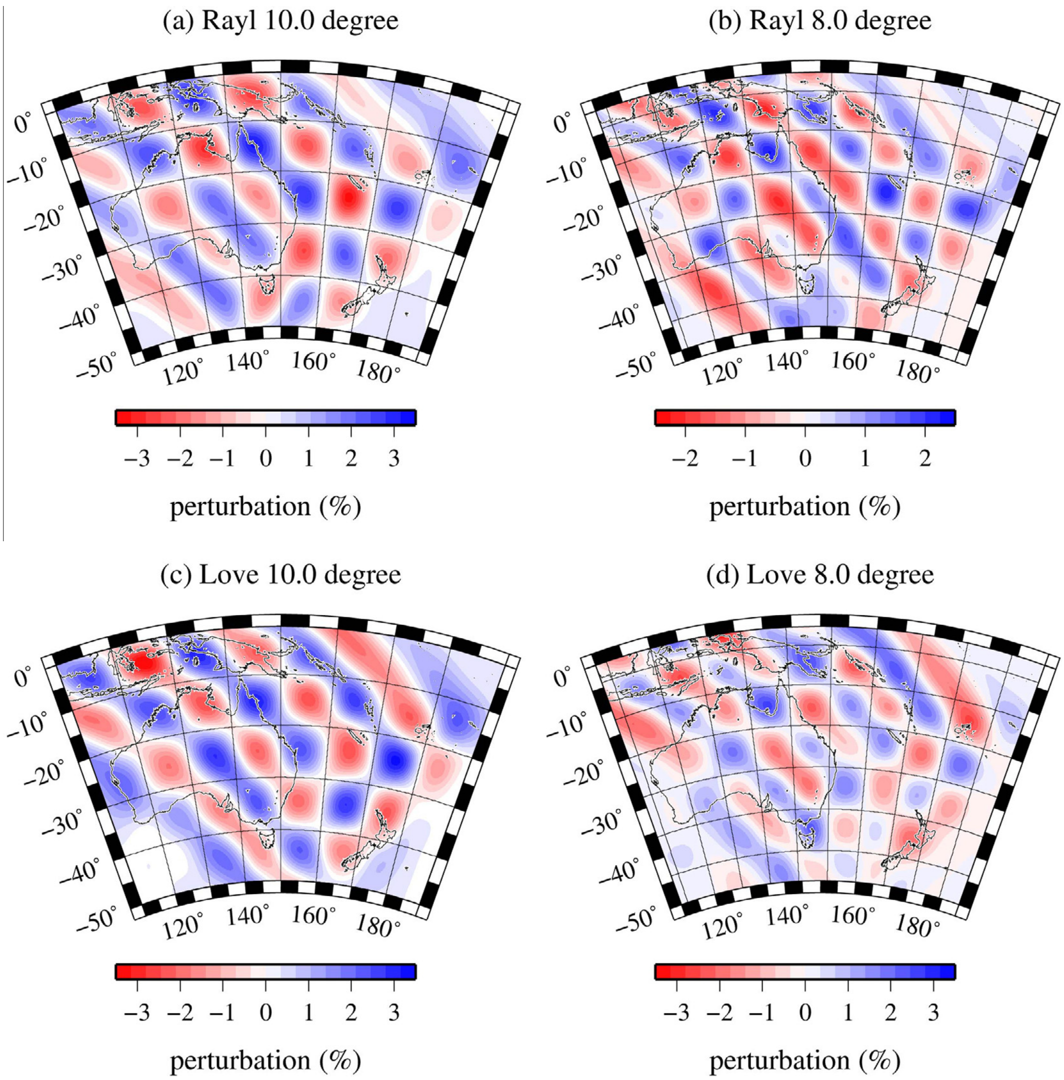

Fig. 7. Results of checkerboard tests for the 2nd higher-mode Rayleigh and Love waves at 100 s period with (a,c) 10.0° cells, (b,d) 8.0° cells.

scaling factors are of secondary importance in the mapping of anisotropic shear wave structure.

In our inversion for velocity structure, the amplitude of the shear wave perturbation and the smoothness of the velocity model are primarily controlled by two a priori parameters; standard deviations σ and a correlation length L, which are used to form the model covariance matrix used in the inversion (e.g., Yoshizawa and Kennett, 2004). In this study, these a priori parameters are set to be $\sigma = 0.05$ km/s and $L = 8$ km in the depth range between Moho and 400 km, and $L = 15$ km between 400 and 670 km. Below 670 km depth, σ is linearly reduced to 0.025, while L is linearly increased to 30 km at 1500 km depth. Crustal velocity is also allowed to be perturbed with $\sigma = 0.025$ km/s and $L = 5$ km, so that rapid variation is allowed in the crust and uppermost mantle, while the deep structure varies smoothly.

4.2. Vertical resolution tests

Examples of vertical resolution tests are displayed in Fig. 8. We create five synthetic models (dashed lines in Fig. 8) including a 5% faster anomaly in a narrow depth range with a varying peak depth from 80 to 300 km, which are used to calculate synthetic dispersion curves for both Love and Rayleigh waves including up to 4th higher modes. The scaling for P wave speeds, density and η parameters are also incorporated in the calculation of synthetic dispersion data. These synthetic data are then inverted for a radially anisotropic shear wave speed profile (solid lines in Fig. 8).

Despite the effects of vertical smearing due to the long-wavelength of surface waves, the input anomaly is recovered well for all the target depths. The retrieved shear wave models with deeper anomalies tend to be smeared more strongly over a wider depth range, and the retrieved wave speed perturbation tends to be underestimated, though we could still achieve a satisfactory recovery of the overall features of input models in the whole upper mantle above the mantle transition zone.

The relative strength of radial anisotropy, which is calculated from the retrieved SV and SH wave speed profiles, is also recovered well in the five synthetic models at our target depth range, with uncertainties of the order of 1–2% or less. This supports our subsequent discussion on the radial anisotropy both in the lithosphere and asthenosphere underneath the Australian continent.

4.3. 3-D shear wave speed model and radial anisotropy

In this study, we consider the isotropic S wave speed model β_{iso}, which is calculated as the Voigt average of the retrieved SV and SH wave speed models (e.g., Panning and Romanowicz, 2006); $\beta_{iso}^2 = (2/3)\ \beta_V^2 + (1/3)\ \beta_H^2$. The final 3-D isotropic S wave speed

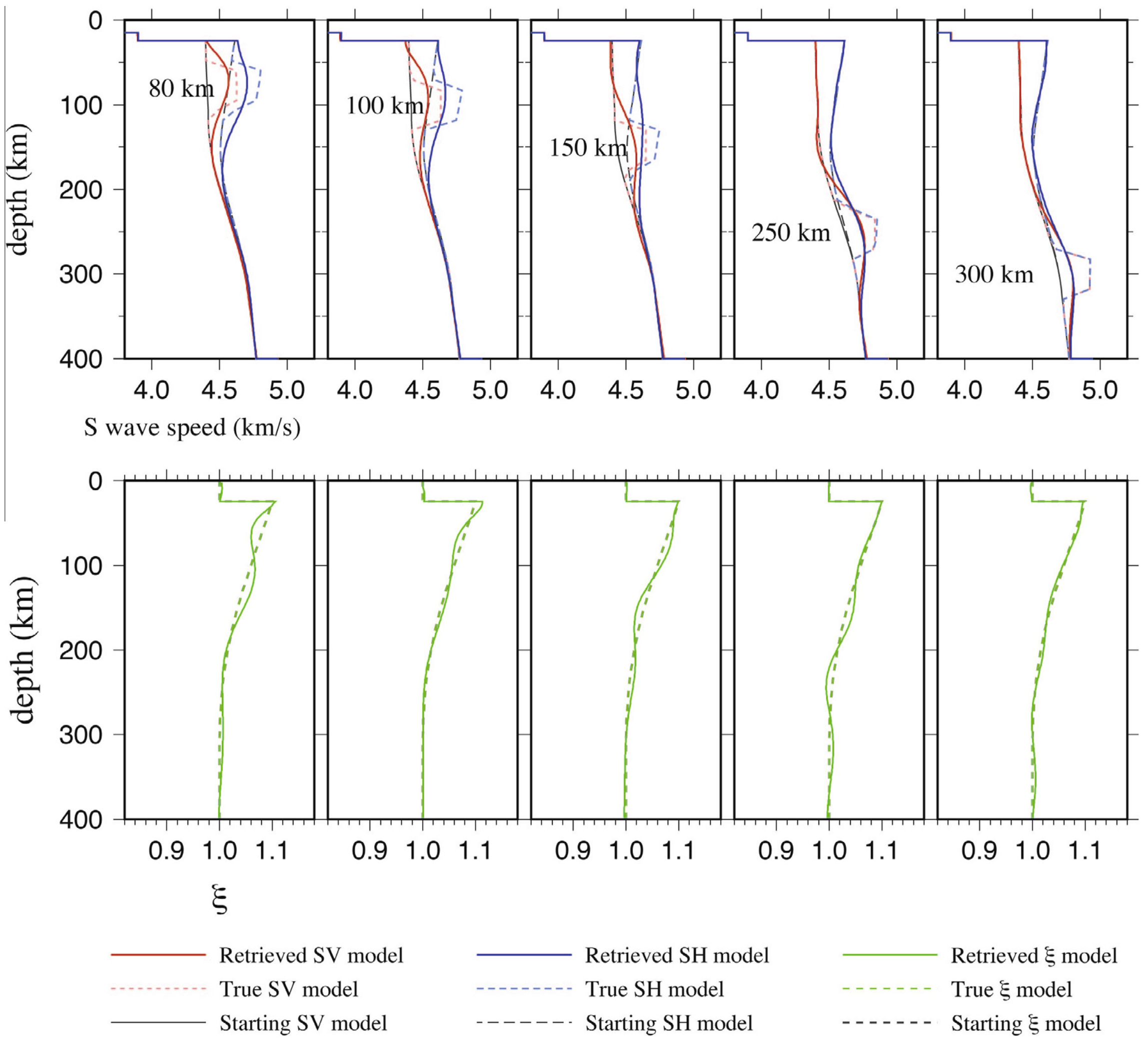

Fig. 8. Examples of vertical resolution tests for the retrieval of anisotropic 1-D shear wave speed models. Synthetic dispersion curves are calculated from the "true" SV and SH models in the top panels, which include a 5% fast anomaly in a narrow depth range (dashed red or blue lines). All the inversions for SV and SH wave speeds are initiated from the starting models (black solid or dashed lines), and retrieved models are plotted with solid red or blue lines. The radial anisotropy parameter ξ in the bottom panels is calculated from the SV and SH wave speed profiles. Note that the starting and true ξ models are the same. (For interpretation of the references to colour in this figure caption, the reader is referred to the web version of this article.)

model as well as radial anisotropy model, $\xi = (\beta_H/\beta_V)^2$, in the Australasian region are displayed in Figs. 9 and 10, respectively. The isotropic S wave speed model is plotted as a perturbation from the regional average 1-D profile shown in Fig. 11, while the radial anisotropy ξ is plotted as a variation from isotropy ($\xi = 1$). The average profiles of the retrieved SV wave speed are fairly close to that of the anisotropic PREM model (gray dashed line in Fig. 11). This is because our Australasian model includes both oceanic and continental regions, and thus the net average profile become closer to the global average. The SH wave speed in the top 150 km is, however, somewhat slower, and the average radial anisotropy ξ is a few per cent smaller than that of PREM in the top 150 km, but about 1–2% larger below this depth. This is likely to reflect regional tectonics of this region that affects the anisotropic properties of the retrieved model. Note that we employed a modified version of anisotropic PREM by smoothing the 220 km discontinuity, and hence the anisotropic depth range is slightly extended to the top 250–300 km.

Major features of our Australian model, such as the fast wave speed in cratonic region in the central and western Australia and the slow anomaly in the Phanerozoic eastern Australia and in the Tasman sea, are consistent with earlier tomographic models of Australia. Very clear correlations of the fast wave speed anomaly with the surface extent of the West and North Australian Cratons are apparent in the isotropic S wave speed models, though such a fast anomaly is not very clear for the South Australian Craton. The anomaly with relatively slower wave speed in central Australia at 75 km depth has been discussed in detail by Fishwick and Reading (2008) and Kennett and Iaffaldano (2013) in conjunction with the prolonged history of deformation, and a highly unusual crustal and lithospheric structures of this region.

In the maps of radial anisotropy (Fig. 10), particularly at around 75 km depth, we can see anomalously strong areas with faster SH wave speed in central Australia along the Mesoproterozoic suture zone among three major cratonic blocks of North, South and West Australian Cratons (Fig. 1), while the anisotropy in the cratons tends to be weaker than its surroundings at shallow depth above 150 km. In these shallower depth, strong fast SH anisotropy can also be found in the east of the Tasman Line in eastern Australia and the Coral Sea. We can also see large-scale anomalous anisotropy with faster SH wave speed in central and northern Australia below 150 km. This feature will be discussed in the subsequent section in combination with the estimated depth of lithosphere–asthenosphere transition.

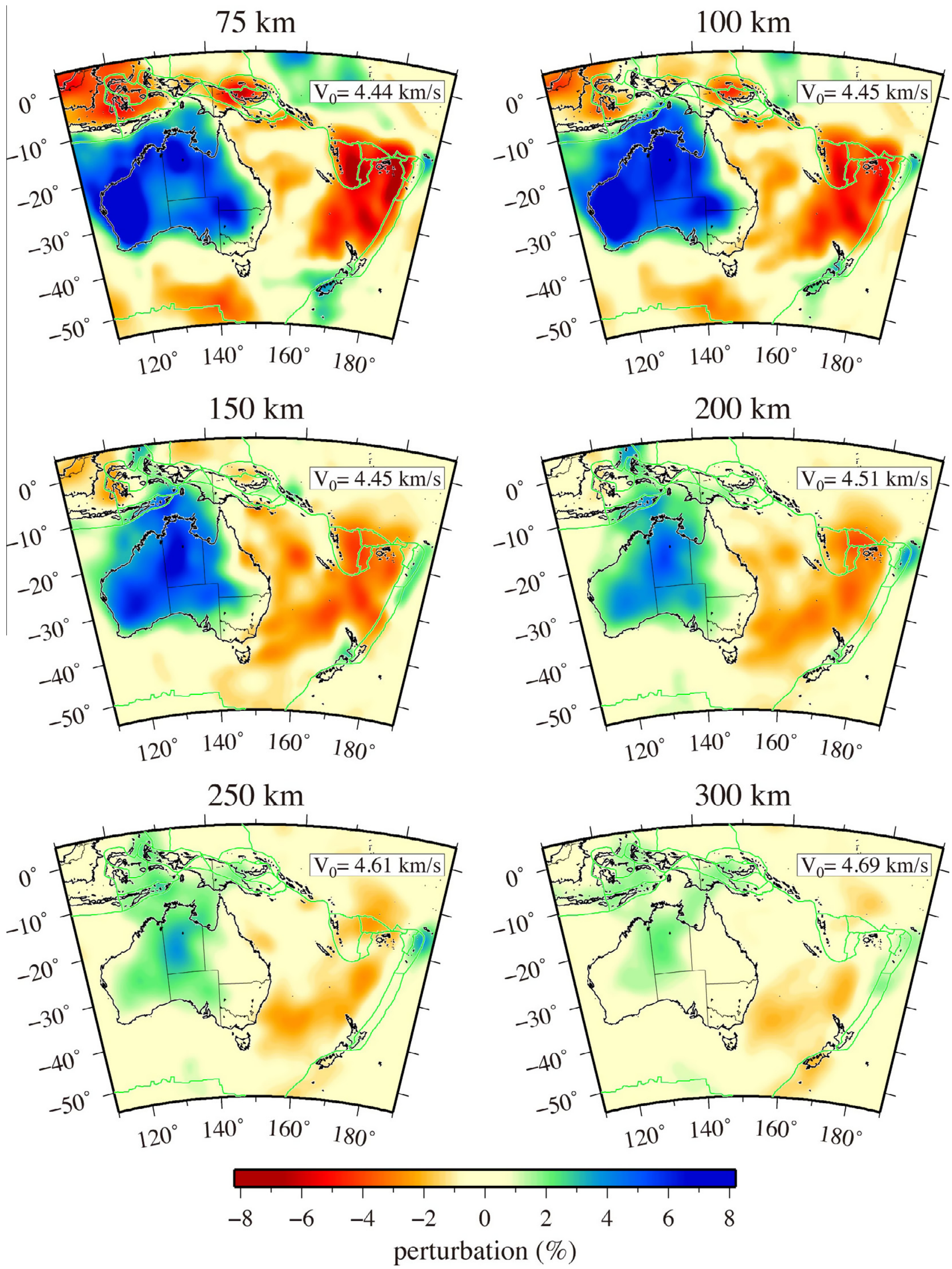

Fig. 9. 3-D isotropic S wave speed models in the Australasian region in the depth range from 75 to 300 km, calculated as the Voigt average of retrieved SV and SH wave speed models. The regional average isotropic S wave speed profile in Fig. 11 (a) at each depth is used as a reference of each map. Plate boundaries are taken from Bird, 2003.

5. Estimating the lithosphere–asthenosphere transition (LAT)

The depth and thickness of the lithosphere–asthenosphere transition are estimated from the combination of a local shear wave speed profile and its vertical gradient. In this study, we employ isotropic S wave speed profiles (or the Voigt average of observed SV and SH wave speeds), for the estimation of the depth and thickness of the LAT.

5.1. Definition of LAT

We consider the LAT not as a single interface, but as a transition zone over a finite depth range, defined by the upper and lower bounds as illustrated in Fig. 12. The depth of the upper bound of LAT, z^U, is estimated from the negative peak of the shear wave speed gradient, while that of the lower bound, z^L, is taken from the slowest shear wave speed in the low velocity zone

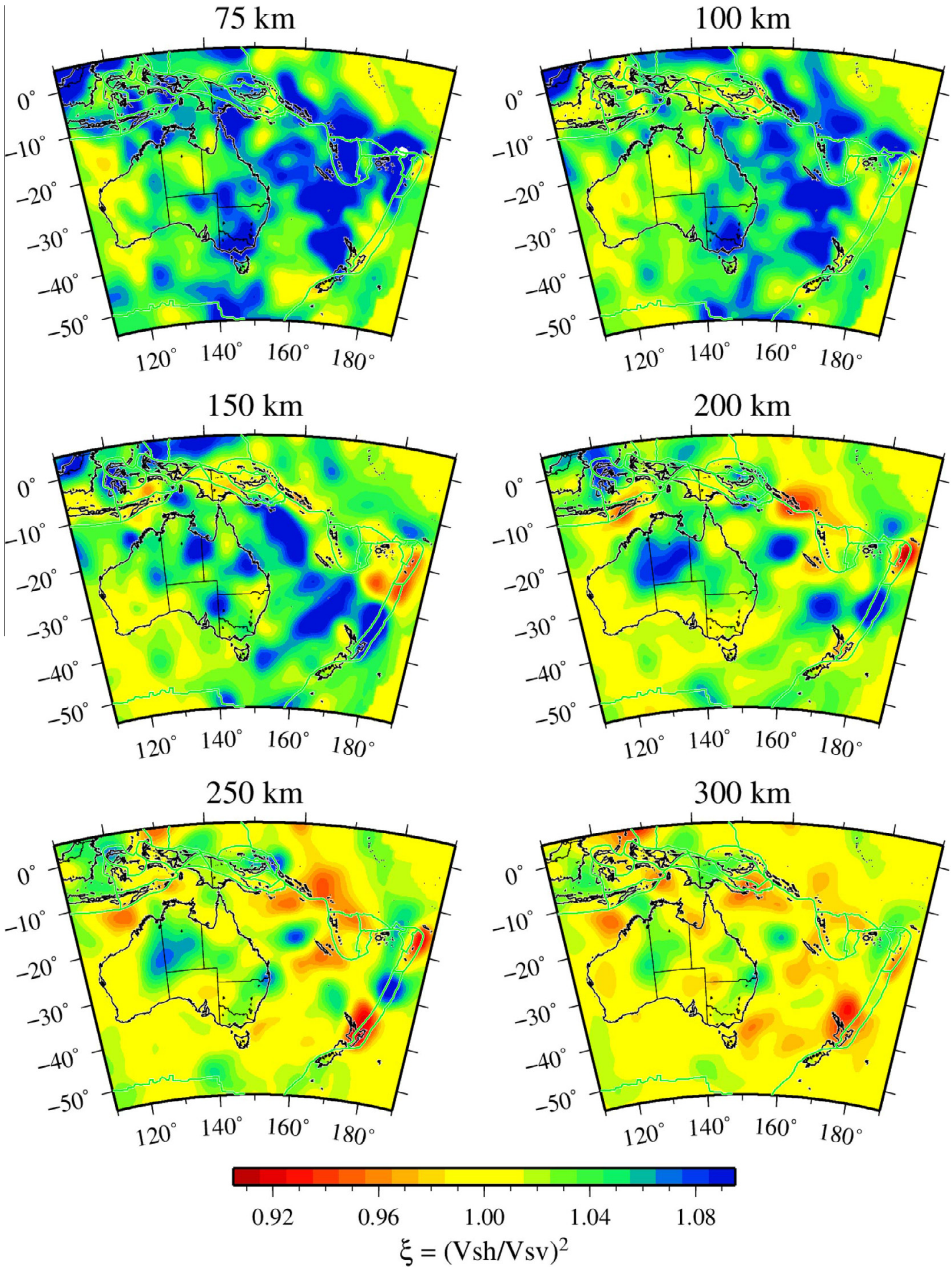

Fig. 10. Same as Fig. 9 but for the anisotropic parameter $\xi = (\beta_H/\beta_V)^2$ plotted as a difference from isotropy ($\xi = 1.0$). ξ is calculated from the retrieved SH and SV wave speed models.

(or the inflection point in the shear wave speed profile). The thickness of the LAT is simply estimated from the difference between the upper and lower bounds, $dz = z^L - z^U$. We also estimate the average velocity gradient in LAT, using the absolute shear velocity at the upper bound, V_S^U, and that at the lower bound, V_S^L. The average velocity drop between the upper and lower bounds of LAT can then be given as $[dV/dz]_{LAT} = (V_S^L - V_S^U)/dz$.

This definition is easily computable and usually appropriate in the estimation of the upper and lower limits of LAT as well as its thickness and average velocity gradient from our local shear wave speed profile across the continental area (Fig. 13). Some locations do not allow the calculation of upper or lower bounds due to a blurred inflection point in our smoothed wave speed profile or multiple negative peaks in velocity gradients, but they can be horizontally interpolated in the mapping process without any significant influence on the prominent features in the final LAT maps.

In the practical application for our shear wave speed model, we have searched for the upper bound of LAT z^U (i.e., the depth of the negative peak in the velocity gradient) in the depth range between z^U_{min} and z^U_{max}, and the lower bound of LAT z^L (i.e., the depth of the slowest wave speed) between z^L_{min} and z^L_{max}. In this study, z^U_{max} and z^L_{max} are set to be 200 and 300 km, respectively. z^U_{min} is taken

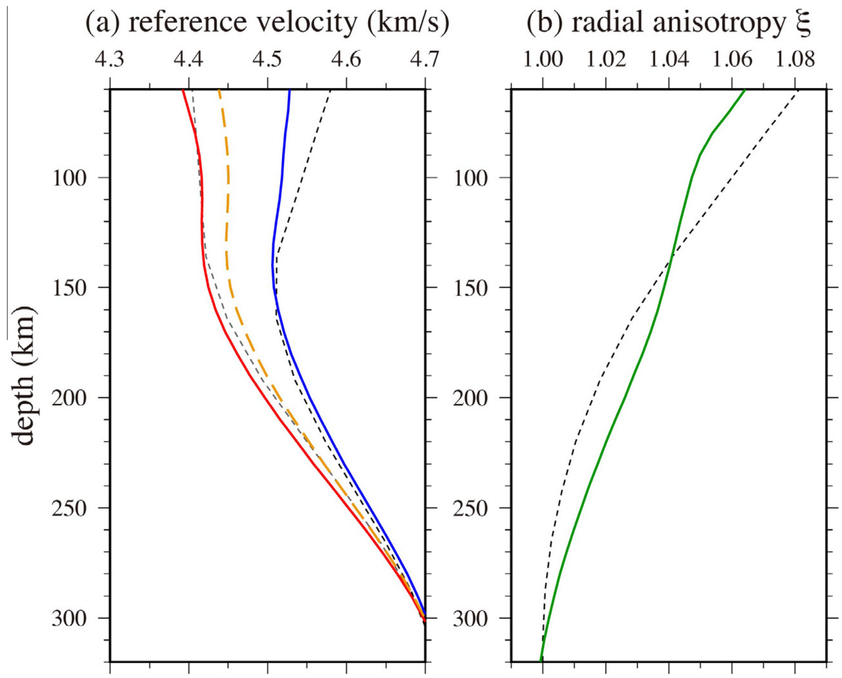

Fig. 11. (a) The velocity profiles of average SV (red solid line) and SH (blue solid line) wave speed of Australian region, the isotropic (Voigt average) S wave speed (orange long-dashed line) used as a reference model in Figs. 9 and 15, and the SH and SV wave speeds of anisotropic PREM (dashed lines) with a smoothed boundary at 220 km depth. (b) The average profile of radial anisotropy ξ (green solid lines) calculated from the SV and SH wave speed in (a), and ξ of anisotropic PREM (dashed line). (For interpretation of the references to colour in this figure legend, the reader is referred to the web version of this article.)

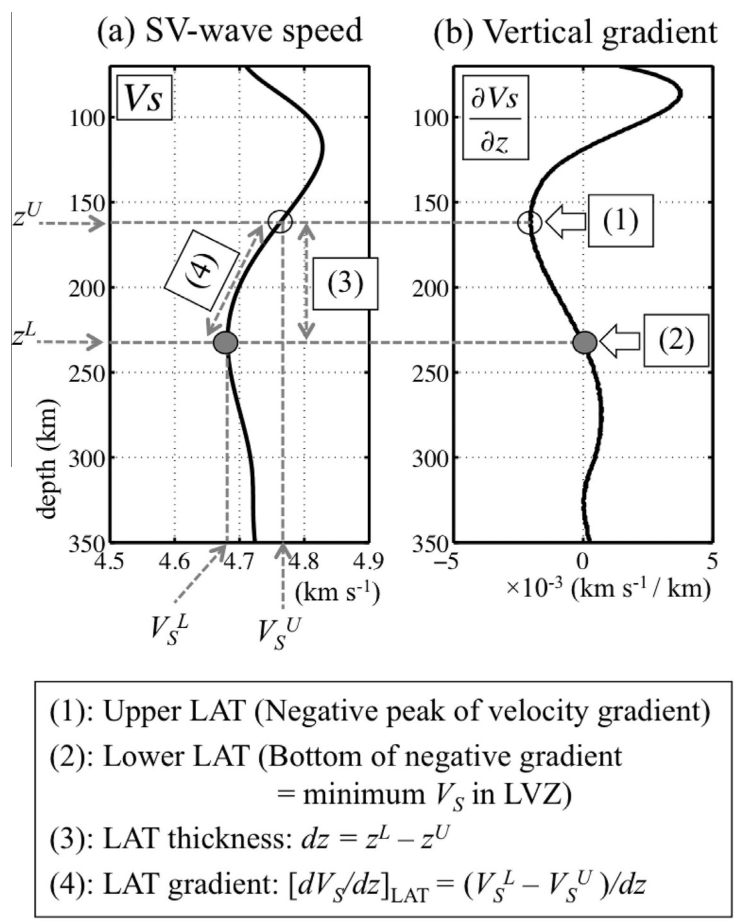

Fig. 12. An example of (a) a shear wave speed profile and (b) its vertical gradient used to estimate the depth of (1) upper and (2) lower bounds of the lithosphere–asthenosphere transition (LAT). (3) The thickness of the LAT, estimated from the difference between (1) and (2). (4) The average velocity gradient in the LAT, calculated from the differences between absolute velocities at upper and lower bounds divided by the thickness.

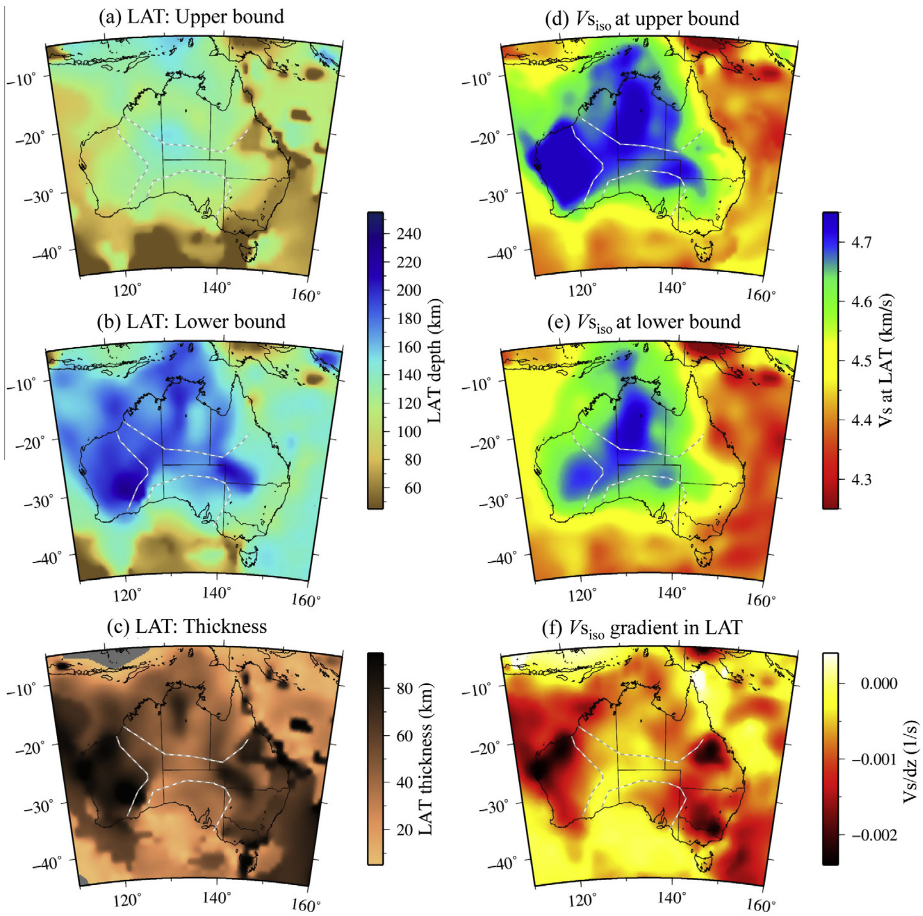

Fig. 13. The depth and thickness of the lithosphere–asthenosphere transition (LAT) across Australia estimated from the vertical velocity gradient of the isotropic S wave speed model. (a) Upper bound, (b) lower bound, and (c) thickness of the LAT. (d) Absolute isotropic S wave speed at upper bound and (e) that at lower bound of LAT, and (f) velocity gradient (or velocity drop) between the upper and lower bounds of LAT.

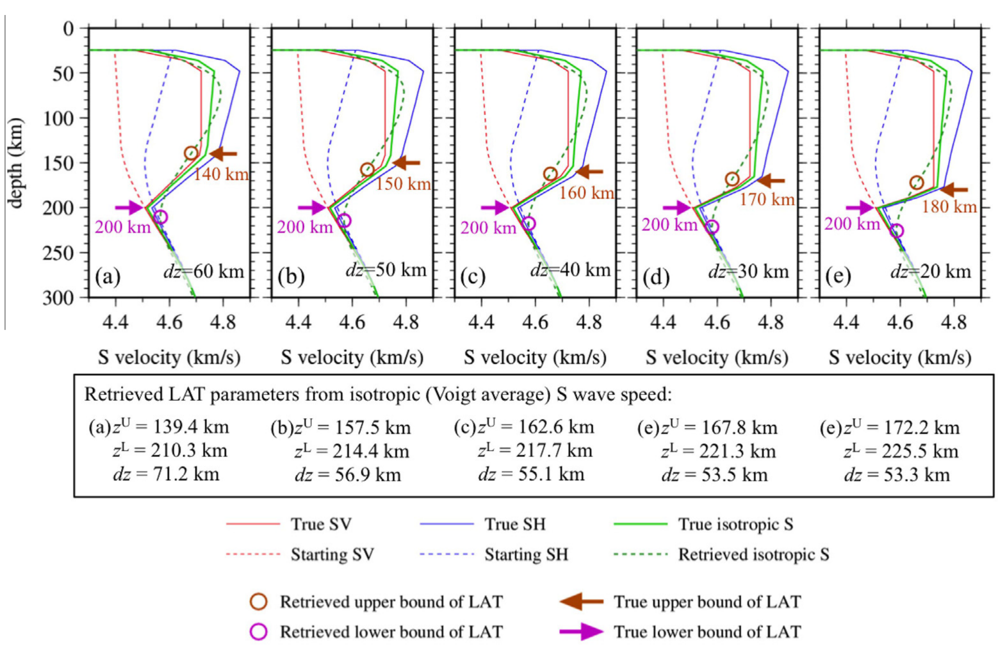

Fig. 14. Synthetic experiments for the retrieval of the upper and lower bounds of the LAT. Brown arrows indicate the upper bounds in the synthetic models, varying from (left) 140 km to (right) 180 km depth, and purple arrows the lower bounds fixed to 200 km depth. Brown and purple circles represent the estimated upper and lower bounds of LAT, respectively, derived from the retrieved isotropic S wave model (green dashed line), which is calculated as the Voigt average of the retrieved SV and SH wave speed models (not shown). The estimated depths of upper and lower bounds as well as the thickness of LAT are summarized below each plot. The starting SV and SH models for the inversions of synthetic data are shown as the red and blue dashed lines, respectively. The solid red and blue lines are the true SV and SH wave speeds used to calculate the isotropic S wave speeds in the green solid line. (For interpretation of the references to colour in this figure legend, the reader is referred to the web version of this article.)

from the larger value of either 35 km or Moho depth +5 km, depending on location, and $z^L_{min} = z^U_{min} + 10$ km.

It should be noted that SV wave speed profiles can also be used to estimate LAT without any significant differences (see the second section of electronic supplement). In contrast, SH wave speed profiles do not provide us with a meaningful estimate of LAT with our simple definition, since they often do not involve a very clear low velocity zone beneath the fast wave speed anomalies of the continental lithosphere. This is consistent with the earlier work on continental radial anisotropy by Gung et al. (2003), which suggests that shear flow in the asthenosphere tends to affect the apparent thickness of the continental lithosphere in SH models.

5.2. LAT recovery tests

Fig. 14 displays the results of synthetic experiments for the retrieval of the upper and lower bounds of the lithosphere–asthenosphere transition with different LAT thickness. The method employed for the synthetic tests is basically the same as for the vertical resolution tests in Fig. 8. For these LAT recovery tests, we create synthetic LAT models by modulating the uppermost mantle of anisotropic PREM incorporating the average feature of our Australian shear wave model; i.e., imposing 7% faster SV wave speed β_V and SH wave speed is calculated from somewhat weakened radial anisotropy with $\beta_H = \sqrt{\xi'}\beta_V$, where $\xi' = 1.0 + (\xi_0 - 1.0) \times 0.7$ (i.e., 70% of original radial anisotropy ξ_0 in PREM). In the 5 synthetic models shown in Fig. 14, the lower bound of the input LAT is fixed at 200 km depth, while the upper bounds are varied from 140 km to 180 km, so that the apparent thickness of the LAT of input model is varied from 20 to 60 km. The synthetic dispersion curves for Love and Rayleigh waves including up to the fourth higher modes are calculated from these synthetic velocity models, which are then inverted for the SV and SH wave speed profiles as in the similar way to the inversions for the observed data. We used the isotropic (Voigt average) S wave speed profile to estimate the upper and lower bounds of LAT.

For a smooth LAT (Fig. 14(a)–(d)) with a thickness of 40 km or greater, both the upper and lower bounds are recovered well and the estimated thickness is close to the true value within the errors of about 10–15 km. The thickness estimates tend to be worse for a sharper boundary with a thickness less than 40 km, since surface waves are intrinsically insensitive to the sharpness of the boundary (Bartzsch et al., 2011). In all cases of synthetic models, the upper bounds are recovered fairly well, suggesting that the definition of the vertical gradient peak provide us with a meaningful depth estimate regarding the transition from lithosphere to asthenosphere. The retrieved thickness of LAT becomes larger for a smoother LAT model, while it gets smaller for a sharper LAT model, indicating that the relative variations of the estimated LAT thickness can be used to infer the regional variations of the LAT sharpness, as long as the LAT thickness is greater than 40 km. Still, care needs to be taken when there is a sharp LAT thinner than 40 km for which the estimated

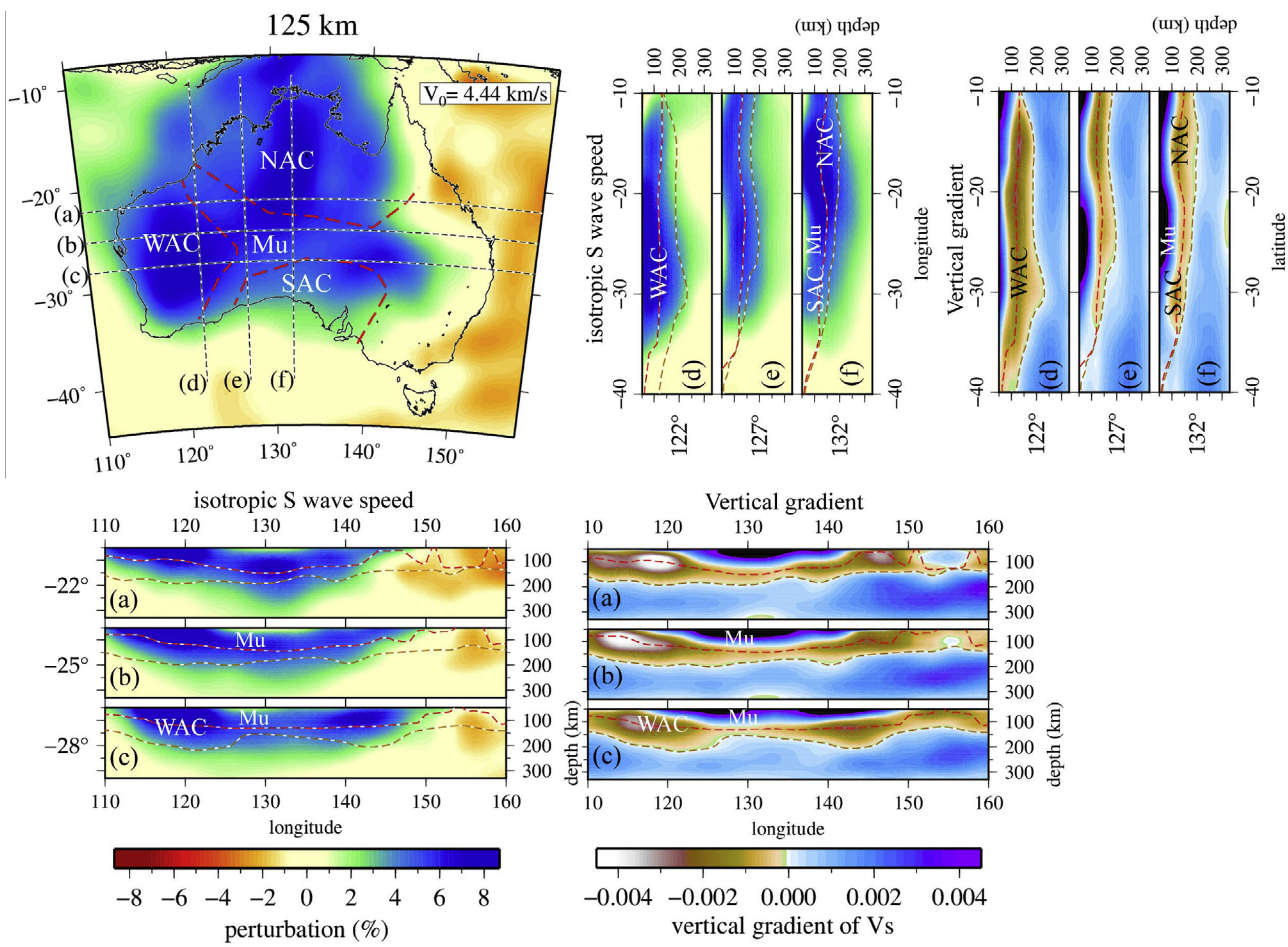

Fig. 15. Isotropic S wave speed model of the Australian continent at 125 km depth and its N–S and E–W cross sections across the center of Australia. Cross sections for vertical gradient of the isotropic S wave speed profile are also shown in the right-hand side. The reference isotropic S wave speed profile is shown in Fig. 11 (a). Thick red dashed lines in the map represent the cratonic boundaries. The upper bound of LAT (red dashed line) and the lower bound of LAT (brown dashed line) are plotted in all the cross sections. WAC: West Australian Craton, NAC: North Australian Craton, SAC: South Australian Craton, Mu: Musgrave Province. (For interpretation of the references to colour in this figure legend, the reader is referred to the web version of this article.)

values of thickness may not be reliable due to the intrinsic lack of sensitivity of surface waves to such a sharp boundary.

It should be noted that the higher modes used in this study are extremely helpful in mapping the base of the thick continental lithosphere (over 200 km in depth), for which just the fundamental mode surface waves start to lose their sensitivity. In fact, when we employ only the fundamental mode in the similar synthetic experiment (results are not shown here), we are not able to retrieve the thickness of LAT properly, even for the case of smooth LAT, as suggested by Bartzsch et al. (2011).

5.3. Continental LAT and radial anisotropy

Maps and cross sections of isotropic S wave speed and radial anisotropy of the continental lithosphere of Australia are displayed in Figs. 15 and 16. We also plot cross sections for vertical gradient of isotropic S wave speed (Fig. 15), which are used to estimate the upper and lower bounds of LAT, represented by dashed lines in all cross sections across the center of Australia.

The upper bound of the LAT (Fig. 13(a)) appears flat across the Archean and Proterozoic regions of the continent, confined in somewhat narrow depth range between 120–150 km. On the contrary, the lower bound of the LAT (Fig. 13(b)) clearly displays large regional variations, ranging from 160 to 250 km, indicating the conspicuously thick lithosphere beneath the Archean cratons of Yilgarn in western Australia, as well as in the center of northern Australia. The thickness of the LAT (Fig. 13(c)) thus becomes larger in the West Australian Craton, while that in South Australian Craton and the Mesoproterozoic suture zone tend to show a relatively thinner LAT.

In cross sections (c), (d) and (f) of Fig. 15, we can trace the thick cratonic lithosphere beneath West and North Australian Cratons, accompanied by the thick transition zone from lithosphere to asthenosphere. On the other hand, the LAT is somewhat thinner in the Mesoproterozoic suture zone in central Australia and South Australian Craton (e.g., cross sections (b), (c), (e) and (f) in Fig. 15).

The radial anisotropy map at 125 km in Fig. 16 exhibits strong anisotropy with faster SH wave speed in eastern Australia, which is apparently separated by the Tasman Line. Moderate size of faster SH wave speed anomaly is also seen near the triple junction among the three cratonic blocks, which merged together about 1.3 Ga (Myers et al., 1996). In the cross sections of radial anisotropy, we can also identify faster SH wave speed anomalies in the asthenosphere beneath the LAT. The moderate anisotropy in the lithosphere is apparently confined in the Mesoproterozoic suture zone between the major cratons, while the anisotropy in the Archean and Proterozoic cratons, particularly around 100 km depth, is relatively weak (Figs. 10 and 16).

Strong radial anisotropy with faster SH is also found in the asthenosphere, particularly in the region with relatively thinner LAT beneath central and northern Australia, which is likely to reflect the horizontal shear flow beneath the fast moving Australian lithosphere as suggested by global studies (e.g., Gung et al., 2003; Debayle et al., 2005). The flow pattern beneath the lithosphere may affect the effective thickness of the LAT beneath central and northern Australia.

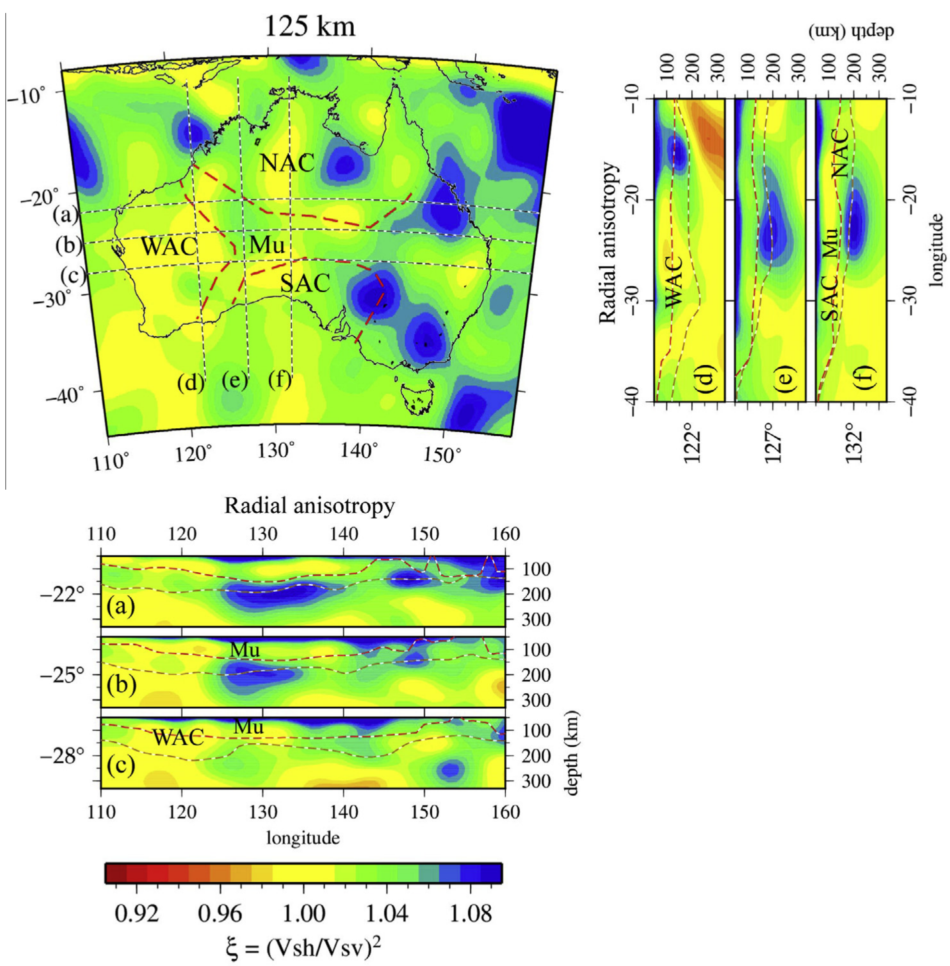

Fig. 16. Same as Fig. 15, but for the anisotropic parameter $\xi = (\beta_H/\beta_V)^2$ plotted as a difference from isotropy ($\xi = 1.0$).

In the cratonic blocks, particularly beneath the Pilbara and Yilgarn Cratons in western Australia and the center of North Australian Cratons, the apparent LAT thickness exceeds 80 km (Figs. 13 and 15). However, the Gawler Craton in south Australia shows distinctly thinner lithosphere and LAT with rather subtle differences from the suture zone in central Australia. Furthermore, the isotropic shear wave speed at upper and lower bounds of LAT beneath this region is apparently slower than the other cratonic region (Fig. 13 (d) and (e)). These differences may indicate the effects of basal erosion during the continental breakup of Australia and Antarctica.

6. Discussion and conclusions

We have constructed a new 3-D radially anisotropic shear wave speed model of Australia, and estimated the lateral variations of the lithosphere–asthenosphere transition from this model. The thickness of LAT and anomalous radial anisotropy indicate intriguing geographical correlations, which may reflect the tectonic history as well as mantle dynamics of this region.

A receiver-function study by Ford et al. (2010) suggests that converted signals generated at the base of the lithosphere can be clearly observed in the eastern half of the Australian continent, but not in the northern and western Australia. This observation is consistent with the estimated thickness as well as the average velocity gradient of LAT in this study; i.e., smoother transition (or thick LAT) is found beneath cratons in northern and western Australia, but sharper (thinner LAT with large velocity gradient) in eastern and southern Australia.

Recent petrological evidence indicates anomalous features of the Musgrave Province, which has been under ultrahigh temperature conditions during 1220–1120 Ma (Smithies et al., 2011) after the amalgamation of three cratonic blocks, which can be explained by the asthenospheric upwelling beneath this area. The Musgrave Province has also undergone several cycles of deformation (Kennett and Iaffaldano, 2013), and thus the anomalous anisotropy found in this area may manifest the prolonged history of formation and deformation of the lithospheric mantle of this local area.

Based on geodynamic modeling in 3D spherical-shell geometry, Yoshida (2012) has shown that the longevity of the cratonic lithosphere depends more strongly on the viscosity contrasts between the cratonic lithosphere and its surroundings, than the high viscosity of the cratonic lithosphere itself. This viscosity contrast requires weak continental margins (e.g., orogenic belts) to protect the cratonic lithosphere from being entrained by surrounding convective forces. The similar result has also been reported by Lenardic et al. (2000) based on 2-D geodynamic modeling. Such a buffering effect may provide a clue for explaining why the Archean cratons in western Australia still keep their rigid continental keels, while their eastern margin (i.e., Musgrave Province) has undergone complex deformation.

The importance of the water contents of olivine on the longevity of the cratonic lithosphere has been pointed out by Peslier et al. (2010), through the analysis of the peridotite xenoliths from the lithosphere–asthenosphere region of the Kaapvaal Craton in South Africa. They suggest that the dry boundary layer at the base of the cratonic lithosphere plays an important role to resist entrainment by the surrounding asthenospheric flow. However, the delamination of such dry cratonic roots may occur if the water content or geotherm is changed by, e.g., a hot upwelling plume. This may explain the differences in the seismic structure of the cratonic lithosphere between west and south Australia; the former keeps its (dry) cratonic root while the latter is likely to have lost it, possibly due to thermal erosion during the breakup of the Australian continent from Antarctica.

Our estimate of the upper and lower bounds of the LAT has been based simply on the 1-D shear wave speed profile. However, our estimate seems to be consistent with the layered cratonic structure found in North America (Yuan and Romanowicz, 2010), which is derived from the depth variations of azimuthal anisotropic properties. Such a layered structure of cratonic lithosphere may be a universal character of cratons, whose full resolution will require further interdisciplinary investigations.

The high resolution anisotropic shear wave model in this paper provides us with insights into the detailed tectonic features of Australia, which cannot readily be obtained from Rayleigh wave information alone. Further progress can be envisaged by the exploitation of the regional seismic networks across the continent; e.g., using inter-station or array-style analysis (e.g., Isse et al., 2006a,Yoshizawa et al., 2010,Bakirci et al., 2012), which will be of help in enhancing the model resolution. The recent deployment of continental-scale portable seismic networks (e.g., USArray in North America and NECESSARRAY in Northeast China) can be of use in the construction of high-resolution models of continental regions. This will enable us to pursue comparative studies on the cratonic lithosphere that can be the basis for unveiling the prolonged tectonic history of continents, including their formation, breakup and amalgamation, and the longevity of the cratons survived through the Wilson cycles.

Acknowledgments

I would like to thank Brian Kennett for numerous discussions, for his comments on an earlier draft of this paper and for the provision of the Australian tectonic map, and Stewart Fishwick and Andreas Fichtner for stimulating discussions on the Australian structure. Constructive comments by an anonymous reviewer were helpful in improving the manuscript. I also thank the IRIS Data Management Center for the provision of broad range of seismic waveform data, and all the members of RSES at the Australian National University who were involved in collecting seismic data through projects of SKIPPY, KIMBA, QUOLL, WACRATON, TIGGER and TASMAL. This study was partly supported by Grant-in-Aid for Scientific Research (Nos. 22654053, 24740298 and 26400443) from the Ministry of Education, Culture, Sports, Science and Technology of Japan.

Appendix A. Supplementary data

Supplementary data associated with this article can be found, in the online version, at http://dx.doi.org/10.1016/j.pepi.2014.07.008.

References

Bakirci, T., Yoshizawa, K., Özer, M.F., 2012. Three-dimensional S-wave structure of the upper mantle beneath Turkey from surface wave tomography. Geophys. J. Int. 190, 1058–1076. http://dx.doi.org/10.1111/j.1365-246X.2012.05526.x.
Bartzsch, S., Lebedev, S., Meier, T., 2011. Resolving the lithosphere–asthenosphere boundary with seismic Rayleigh waves. Geophys. J. Int. 186, 1152–1164.
Bird, P., 2003. An updated digital model of plate boundaries. Geochem. Geophys. Geosyst. 4, 1027. http://dx.doi.org/10.1029/2001GC000252.
Bourova, E., Yoshizawa, K., Yomogida, K., 2010. Upper mantle structure of marginal seas and subduction zones in northeastern Eurasia from Rayleigh wave tomography. Phys. Earth Planet. Inter. 183, 20–32. http://dx.doi.org/10.1016/j.pepi.2010.06.007.
Dahlen, F.A., Tromp, J., 1998. Theoretical Global Seismology. Princeton University Press, Princeton, NJ.
Debayle, E., Kennett, B., Priestley, K., 2005. Global azimuthal seismic anisotropy and the unique plate-motion deformation of Australia. Nature 433, 509–512. http://dx.doi.org/10.1038/nature03247.
Debayle, E., Kennett, B.L.N., 2000a. Anisotropy in the Australasian upper mantle from Love and Rayleigh waveform inversion. Earth Planet. Sci. Lett. 184, 339–351. http://dx.doi.org/10.1016/S0012-821X(00)00314-9.
Debayle, E., Kennett, B.L.N., 2000b. The Australian continental upper mantle: structure and deformation inferred from surface waves. J. Geophys. Res. 105, 25423–25450. http://dx.doi.org/10.1029/2000JB900212.

Fichtner, A., Kennett, B.L.N., Igel, H., Bunge, H.P., 2010. Full waveform tomography for radially anisotropic structure: new insights into present and past states of the Australasian upper mantle. Earth Planet. Sci. Lett. 290, 270–280. http://dx.doi.org/10.1016/j.epsl.2009.12.003.

Fishwick, S., Heintz, M., Kennett, B.L.N., Reading, A.M., Yoshizawa, K., 2008. Steps in lithospheric thickness within eastern Australia, evidence from surface wave tomography. Tectonics 27. http://dx.doi.org/10.1029/2007TC002116.

Fishwick, S., Kennett, B.L.N., Reading, A.M., 2005. Contrasts in lithospheric structure within the Australian craton – insights from surface wave tomography. Earth Planet. Sci. Lett. 231, 163–176. http://dx.doi.org/10.1016/j.epsl.2005.01.009.

Fishwick, S., Rawlinson, N., 2012. 3-D structure of the Australian lithosphere from evolving seismic datasets. Aust. J. Earth Sci 59, 809–826. http://dx.doi.org/10.1080/08120099.2012.702319.

Fishwick, S., Reading, A.M., 2008. Anomalous lithosphere beneath the Proterozoic of western and central Australia: a record of continental collision and intraplate deformation? Precambrian Res. 166, 111–121. http://dx.doi.org/10.1016/j.precamres.2007.04.026.

Ford, H.A., Fischer, K.M., Abt, D.L., Rychert, C.A., Elkins-Tanton, L.T., 2010. The lithosphere–asthenosphere boundary and cratonic lithospheric layering beneath Australia from Sp wave imaging. Earth Planet. Sci. Lett. 300, 299–310. http://dx.doi.org/10.1016/j.epsl.2010.10.007.

Gung, Y., Panning, M., Romanowicz, B., 2003. Global anisotropy and the thickness of continents. Nature 422, 707–711. http://dx.doi.org/10.1038/nature01559.

van der Hilst, R.D., Kennett, B., Christie, D., Grant, J., 1994. Project Skippy explores lithosphere and mantle beneath Australia. Eos Trans. AGU 75, 177. http://dx.doi.org/10.1029/94EO00857.

Isse, T., Suetsugu, D., Shiobara, H., Sugioka, H., Yoshizawa, K., Kanazawa, T., Fukao, Y., 2006a. Shear wave speed structure beneath the South Pacific superswell using broadband data from ocean floor and islands. Geophys. Res. Lett. 33, L16303. http://dx.doi.org/10.1029/2006GL026872.

Isse, T., Yoshizawa, K., Shiobara, H., Shinohara, M., Nakahigashi, K., Mochizuki, K., Sugioka, H., Suetsugu, D., Oki, S., Kanazawa, T., Suyehiro, K., Fukao, Y., 2006b. Three-dimensional shear wave structure beneath the Philippine Sea from land and ocean bottom broadband seismograms. J. Geophys. Res. 111. http://dx.doi.org/10.1029/2005JB003750.

Kennett, B.L.N., Fichtner, A., Fishwick, S., Yoshizawa, K., 2013. Australian seismological reference model (AuSREM): mantle component. Geophys. J. Int. 192, 871–887. http://dx.doi.org/10.1093/gji/ggs065.

Kennett, B.L.N., Iaffaldano, G., 2013. Role of lithosphere in intra-continental deformation: Central Australia. Gondwana Res. 24, 958–968. http://dx.doi.org/10.1016/j.gr.2012.10.010.

Kennett, B.L.N., Yoshizawa, K., 2002. A reappraisal of regional surface wave tomography. Geophys. J. Int. 150, 37–44. http://dx.doi.org/10.1046/j.1365-246X.2002.01682.x.

Lenardic, A., Moresi, L., Mühlhaus, H., 2000. The role of mobile belts for the longevity of deep cratonic lithosphere: the crumple zone model. Geophys. Res. Lett. 27, 1235–1238. http://dx.doi.org/10.1029/1999GL008410.

Montagner, J.P., Anderson, D.L., 1989. Petrological constraints on seismic anisotropy. Phys. Earth Planet. Inter. 54, 82–105. http://dx.doi.org/10.1016/0031-9201(89)90189-1.

Myers, J.S., Shaw, R.D., Tyler, I.M., 1996. Tectonic evolution of proterozoic Australia. Tectonics 15, 1431–1446. http://dx.doi.org/10.1029/96TC02356.

Nataf, H.C., Ricard, Y., 1996. 3SMAC: an a priori tomographic model of the upper mantle based on geophysical modeling. Phys. Earth Planet. Inter. 95, 101–122. http://dx.doi.org/10.1016/0031-9201(95)03105-7.

Panning, M., Romanowicz, B., 2006. A three-dimensional radially anisotropic model of shear velocity in the whole mantle. Geophys. J. Int. 167, 361–379. http://dx.doi.org/10.1111/j.1365-246X.2006.03100.x.

Peslier, A.H., Woodland, A.B., Bell, D.R., Lazarov, M., 2010. Olivine water contents in the continental lithosphere and the longevity of cratons. Nature 467, 78–81. http://dx.doi.org/10.1038/nature09317.

Sambridge, M., 1999. Geophysical inversion with a neighbourhood algorithm-I. Searching a parameter space. Geophys. J. Int. 138, 479–494. http://dx.doi.org/10.1046/j.1365-246X.1999.00876.x.

Simons, F.J., van der Hilst, R.D., Montagner, J.P., Zielhuis, A., 2002. Multimode Rayleigh wave inversion for heterogeneity and azimuthal anisotropy of the Australian upper mantle. Geophys. J. Int. 151, 738–754. http://dx.doi.org/10.1046/j.1365-246X.2002.01787.x.

Smithies, R.H., Howard, H.M., Evins, P.M., Kirkland, C.L., Kelsey, D.E., Hand, M., Wingate, M.T.D., Collins, A.S., Belousova, E., 2011. High-temperature granite magmatism, crust–mantle interaction and the mesoproterozoic intracontinental evolution of the Musgrave Province, Central Australia. J. Petrol. 52, 931–958. http://dx.doi.org/10.1093/petrology/egr010.

Takeuchi, H., Saito, M., 1972. Seismic surface waves. In: Bolt, B.A. (Ed.), Seismology: Surface Waves and Free Oscillations. Academic Press, New York, pp. 217–295.

Tarantola, A., Valette, B., 1982. Generalized nonlinear inverse problems solved using the least squares criterion. Rev. Geophys. Space Phys. 20, 219–232.

Yoshida, M., 2012. Dynamic role of the rheological contrast between cratonic and oceanic lithospheres in the longevity of cratonic lithosphere: a three-dimensional numerical study. Tectonophysics 532–535, 156–166. http://dx.doi.org/10.1016/j.tecto.2012.01.029.

Yoshizawa, K., Ekström, G., 2010. Automated multimode phase speed measurements for high-resolution regional-scale tomography: application to North America. Geophys. J. Int. 183, 1538–1558. http://dx.doi.org/10.1111/j.1365-246X.2010.04814.x.

Yoshizawa, K., Kennett, B.L.N., 2002a. Determination of the influence zone for surface wave paths. Geophys. J. Int. 149, 440–453. http://dx.doi.org/10.1046/j.1365-246X.2002.01659.x.

Yoshizawa, K., Kennett, B.L.N., 2002b. Non-linear waveform inversion for surface waves with a neighbourhood algorithm–application to multimode dispersion measurements. Geophys. J. Int. 149, 118–133. http://dx.doi.org/10.1046/j.1365-246X.2002.01634.x.

Yoshizawa, K., Kennett, B.L.N., 2004. Multimode surface wave tomography for the Australian region using a three-stage approach incorporating finite frequency effects. J. Geophys. Res. 109, B02310. http://dx.doi.org/10.1029/2002JB002254.

Yoshizawa, K., Miyake, K., Yomogida, K., 2010. 3D upper mantle structure beneath Japan and its surrounding region from inter-station dispersion measurements of surface waves. Phys. Earth Planet. Inter. 183, 4–19. http://dx.doi.org/10.1016/j.pepi.2010.02.012.

Yuan, H., Romanowicz, B., 2010. Lithospheric layering in the North American craton. Nature 466, 1063–1068. http://dx.doi.org/10.1038/nature09332.